Ambiguities Suppression for Azimuth Multichannel SAR Based on $L_{2,q}$ Regularization With Application to Gaofen-3 Ultra-Fine Stripmap Mode

Mingqian Liu, Bingchen Zhang, Zhongqiu Xu, Yan Zhang, Lihua Zhong, and Yirong Wu, *Member, IEEE*

***Abstract*—The azimuth multichannel synthetic aperture radar (SAR) technology is capable of overcoming the minimum antenna area constraint and achieving high-resolution and wide-swath (HRWS) imaging. Generally speaking, the pulse repetition frequency (PRF) of the spaceborne multichannel SAR systems should satisfy the azimuthal uniform sampling condition, but it is sometimes impossible due to the limitation of radar system timing conditions, which is often referred as "coverage diagram." For the Gaofen-3 system, the PRF of each channel at some beam positions is slightly less than that of uniform sampling in the dual-channel mode, leading to the nonuniform undersampling, hence, resulting the azimuth ambiguities in the recovered images. Although the ambiguous energy in Gaofen-3 images is not high in general, it is still noticeable amid surrounding weak clutters of strong targets. In this article, a novel multichannel SAR imaging method for nonuniform undersampling based on $L_{2,q}$ regularization $(0 < q \leq 1)$ is proposed. By analyzing the reasons of azimuth ambiguities in the multichannel SAR system, the imaging model is established with emphasizing the difference from conventional single-channel SAR. Then, we combine the multichannel SAR data processing operators with the group sparsity property to construct the novel imaging method. The group sparsity property is modeled by the $2, q$-norm, and the $L_{2,q}$ regularization problem can be solved via sparse group thresholding function. It is shown that the proposed method can efficiently suppress the azimuth ambiguities caused by nonuniform undersampling. Simulations and Gaofen-3 real data experiments are exploited to verify the effectiveness of the proposed method.**

***Index Terms*—Azimuth ambiguity, compressive sensing (CS), Gaofen-3, $L_{2,q}$ regularization, multichannel synthetic aperture radar (SAR).**

Manuscript received October 7, 2020; revised December 1, 2020; accepted December 17, 2020. Date of publication December 21, 2020; date of current version January 8, 2021. This work was supported by the National Natural Science Foundation of China under Grant 61991421. *(Corresponding author: Mingqian Liu.)*

Mingqian Liu, Zhongqiu Xu, Yan Zhang, and Yirong Wu are with the Aerospace Information Research Institute, Chinese Academy of Sciences, Beijing 100094, China also with the Key Laboratory of Technology in Geo-Spatial Information Processing and Application System, Chinese Academy of Sciences, Beijing 100190, China, and also with School of Electronic, Electrical and Communication Engineering, University of Chinese Academy of Sciences, Beijing 101408, China (e-mail: liumingqian171@mails.ucas.ac.cn; xuzhongqiu18@mails.ucas.ac.cn; zhangyan18@mails.ucas.ac.cn; wyr@mail.ie.ac.cn).

Bingchen Zhang and Lihua Zhong are with the Aerospace Information Research Institute, Chinese Academy of Sciences, Beijing 100094, China also with School of Electronic, Electrical and Communication Engineering, University of Chinese Academy of Sciences, Beijing 101408, China (e-mail: zhangbc@aircas.ac.cn; lhzhong3@163.com).

Digital Object Identifier 10.1109/JSTARS.2020.3046366

I. Introduction

SYNTHETIC aperture radar (SAR) is an important remote sensing technology that can work in all-weather and all-time, and has been widely applied into many fields such as marine surveillance, agricultural production monitoring, and target detection [1]–[4]. For traditional single-channel SAR systems, azimuth resolution and swath width cannot be increased at the same time since they are mutually restricted. As an innovative imaging technology, the azimuth multichannel SAR system overcomes the inherent limitation of minimum antenna area constraint and can simultaneously achieve high-resolution and wide-swath (HRWS) imaging [5]–[7]. For best performance, the pulse repetition frequency (PRF) of the multichannel SAR system should be chosen so that the platform moves only one half of its total length between subsequent transmitted pulses, resulting in the azimuthal uniform sampling. However, limited by the beam position design of some spaceborne multichannel SAR systems, the actual PRF will deviate from such rigidly selected uniform PRF, and cause nonuniform sampling in practice. In case the PRF of each channel is less than that of uniform sampling (see Fig. 1), the equivalent azimuth sampling rate will be less than the Doppler bandwidth after azimuth spectrum reconstruction, hence, result in the nonuniform undersampling, which makes the problem even worse.

Gaofen-3 is a *C*-band SAR (5.4 GHz) satellite of China's high-resolution earth observation project, which was launched in August 2016 [8]. Gaofen-3 is also the first Chinese spaceborne azimuth multichannel SAR system working in the ultra-fine stripmap (UF) mode, i.e., the dual-channel mode [9]. However, the PRF of each channel in the Gaofen-3 dual-channel mode is slightly less than the uniform PRF under some specific beam positions, resulting azimuth ambiguities. Although the ambiguous energy is generally low, for some strong targets such as the ships on the sea, the ambiguous energy could be higher than the surrounding clutter hence affect the image quality. Therefore, their ambiguities need to be suppressed.

In [10], Krieger *et al.* proposed a multichannel spectrum reconstruction algorithm based on the filter bank to solve the nonuniform sampling problem. This algorithm is developed from generalized sampling theorem [11]. When the Nyquist criterion is fulfilled, the azimuth spectrum can be reconstructed unambiguously by solving a linear system of equations. However, for the nonuniform undersampling situation, this algorithm is no longer applicable and will give rise to aliases in the

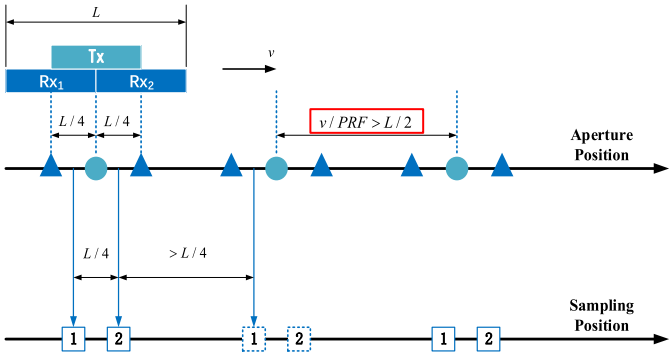

Fig. 1. Example of the nonuniform undersampling scheme (dual-channel mode).

reconstructed signal. The recovered images will suffer from serious azimuth ambiguities [12].

In recent years, the sparse signal processing methods based on compressive sensing (CS) theory [13], [14] have been applied to SAR imaging [15], [16]. The target scene can be reconstructed by solving L_q $(0 < q \leq 1)$ regularization problem, which has already been used in some imaging modes in the single-channel SAR system [17], [18]. In [19], Quan *et al.* introduced L_q regularization into multichannel SAR signal reconstruction to solve the azimuth ambiguities caused by nonuniform sampling. However, the L_q-regularization-based method did not consider the joint structure of the SAR signal, which reflects the intersignal correlation [20], and cannot deal with the azimuth ambiguities brought by the nonuniform undersampling. Recently, $L_{2,q}$ regularization has been applied to azimuth ambiguities suppression of single-channel SAR imaging [21]. This method first construct the single-channel sparse SAR imaging model with azimuth ambiguities; then the group sparsity constraint is imposed in the sparse SAR imaging model to tackle azimuth ambiguities based on the fact that the main imaging area and ambiguous areas share the same signal support set. Thus, compared with the L_q-regularization-based method, the $L_{2,q}$-regularization-based method can reconstruct scene of interest more accurately, and it can be further applied to multichannel SAR imaging.

In this article, we propose a novel multichannel SAR imaging method for nonuniform undersampling condition inspired by $L_{2,q}$ regularization. The proposed method is capable of suppressing the azimuth ambiguities and noise, and its main advantages and contributions are summarized as follows.

1) Compared with the single-channel imaging model [21], this article analyzes the reasons of azimuth ambiguities in the multichannel SAR system and develops the sparse SAR imaging model that varies from [21]. Moreover, different from the single-channel SAR imaging operators, the multichannel SAR imaging operators in this article not only take the monostatic SAR imaging into consider, but also the Doppler spectrum reconstruction.
2) Compared with the L_q-regularization-based method in [19], the proposed method considers both the main imaging area and ambiguous areas when deriving the sparse SAR imaging model, and introduces the group sparsity property into multichannel SAR data processing. Therefore, the proposed method can suppress the noise as well as the azimuth ambiguities caused by nonuniform undersampling.
3) The Gaofen-3 system suffers from the nonuniform undersampling in the dual-channel mode under some beam positions. In this article, we adopt the proposed method in the scene of sparse sea surface, achieving the azimuth ambiguities suppression of ship targets and improving the imaging quality.

The rest of this article is organized as follows. Section II briefly introduces the L_q-regularization-based multichannel SAR imaging method for nonuniform sampling. Section III analyzes the factors of azimuth ambiguities in the nonuniform undersampling multichannel SAR system, develops the novel sparse SAR imaging model, and introduces the proposed $L_{2,q}$-regularization-based multichannel SAR imaging method in detail. The numerical simulations and Gaofen-3 dual-channel mode real data experiments are exploited in Section IV to demonstrate the effectiveness of the proposed method. Section V finally concludes this article.

II. L_q-Regularization-Based Multichannel SAR Imaging Method for Nonuniform Sampling

A. Observation-Matrix-Based Sparse SAR Imaging Model

Considering an azimuth multichannel SAR system, the echo data of its jth channel can be expressed as follows:

$$y_j(t,\tau) = \iint_{(p,q)\in\mathbb{C}^b} x(p,q)\cdot\omega_a\left(t-\frac{p}{v}\right)\cdot \exp\left\{-j\frac{2\pi}{\lambda}\left(R(p,q,t)+R_j(p,q,t)\right)\right\} \cdot s\left(\tau-\frac{R(p,q,t)+R_j(p,q,t)}{c}\right)dpdq, \quad (1)$$

where $\mathbb{C}^b$ is the observed scene; t and τ are azimuth time and range time, respectively; p and q are the indices of azimuth and range coordinates of the observed target, respectively; $x(\cdot)$ is the backscattered coefficient of the target; $\omega_a(\cdot)$ is the azimuth antenna weight; v is the velocity of the platform; c is the speed of light; $R(p,q,t)$ is the distance from the transmitter to the target; $R_j(p,q,t)$ is the distance from the jth receiver to the target; λ is the carrier wavelength. and $s(\cdot)$ is the transmitted pulse signal.

Let $\mathbf{Y}\in\mathbb{C}^{N_a\times N_r}$ denote the multichannel two-dimensional (2-D) echo data, and $\mathbf{y} = \mathrm{vec}(\mathbf{Y})\in\mathbb{C}^{N\times 1}$ is the vectorized version of $\mathbf{Y}$, where $N = N_a$ (azimuth) $\times N_r$(range) and $\mathrm{vec}(\cdot)$ is the vectorization operator. Let $\mathbf{Y}_j\in\mathbb{C}^{N_a/M\times N_r}$ represent the 2-D echo data of the jth channel, where M is the number of channels and $\mathbf{y}_j = \mathrm{vec}(\mathbf{Y}_j)\in\mathbb{C}^{L\times 1}$ with $L = N_a \times N_r/M$. Discretizing model (1) in temporal domain T_l $(l = 1, 2, \ldots, L)$, we can get the discrete model

$$\mathbf{y}_j = \sum_{l=1}^{L}\sum_{n=1}^{N}\phi^j(l,n)\ x(p_n,q_n) \quad (2)$$

where $\phi^j(\cdot)$ is the observation matrix of the jth channel, denoted as follows:

$$\phi^j(l,n) = \iint_{(t,\tau)\in T_l} \omega_a\left(t-\frac{p_n}{v}\right) \cdot s\left(\tau - \frac{R(p_n,q_n,t)+R_j(p_n,q_n,t)}{c}\right) \cdot \exp\left\{-j\frac{2\pi}{\lambda}\left(R(p_n,q_n,t)+R_j(p_n,q_n,t)\right)\right\} dtd\tau. \quad (3)$$

Let $\mathbf{y} = [\boldsymbol{y}_1{}^T, \boldsymbol{y}_2{}^T, \ldots, \boldsymbol{y}_M{}^T]^T$, where $\mathbf{y}_j$ is the echo data vector of the jth channel. Let $\mathbf{X} \in \mathbb{C}^{N_a \times N_r}$ denote the 2-D backscattered coefficient matrix of the observed scene and $\mathbf{x} = \mathrm{vec}(\mathbf{X}) \in \mathbb{C}^{N\times 1}$. Then the observation-matrix-based sparse SAR imaging model can be expressed as [15], [19] follows:

$$\mathbf{y} = \mathbf{\Phi}\mathbf{x} + \mathbf{n} \quad (4)$$

where $\mathbf{\Phi} = [\phi^1; \phi^2; \ldots, \phi^M]$ is the observation matrix of the multichannel SAR system with M channels, and $\mathbf{n} \in \mathbb{C}^{N\times 1}$ is the additive noise vector.

B. L_q-Regularization-Based Reconstruction Method

For the noisy imaging model (4), if the scene of interest $\mathbf{x}$ is sparse enough and the observation matrix $\mathbf{\Phi}$ satisfies the restricted isometry property (RIP) [22] condition, $\mathbf{x}$ can be recovered by solving the L_q regularization problem

$$\hat{\mathbf{x}} = \underset{\mathbf{x}}{\mathrm{argmin}} \left\{\|\mathbf{y}-\mathbf{\Phi}\mathbf{x}\|_2^2 + \lambda\|\mathbf{x}\|_q^q\right\} \quad (5)$$

where λ is the regularization parameter of the $\|\mathbf{x}\|_q$ term, and $\|\mathbf{x}\|_q$ can be expressed as follows:

$$\|\mathbf{x}\|_q = \left(\sum_{n=1}^{N} \left(|\mathbf{x}(n)|\right)^q\right)^{\frac{1}{q}}. \quad (6)$$

To solve (5), we adopt the iterative soft thresholding algorithm [23]. The iterative solution process can be represented as follows:

$$\mathbf{x}^{(k+1)} = \eta_{q,\lambda\mu}\left(\mathbf{x}^{(k)} + \mu\mathbf{\Phi}^H\left(\mathbf{y}-\mathbf{\Phi}\mathbf{x}^{(k)}\right)\right) \quad (7)$$

where $\eta_{q,\lambda\mu}(\cdot)$ is the soft thresholding function and μ is the step size controlling the convergence speed of the soft thresholding algorithm. After reconstruction, the vector $\hat{\mathbf{x}}$ should be transferred to the form of matrix.

However, considering that the observation-matrix-based sparse SAR imaging depends on vectorizing the echo data matrix to implement decoupling and contains matrix-vector multiplication operations, it will require huge computational and memory costs. Therefore, according to the idea of approximated observation [17], we replace the observation matrix $\mathbf{\Phi}$ with the multichannel SAR echo generation operator $\mathcal{G}_j(\cdot)$ [19]. Corresponding to (7), the iterative solution process can be rewritten as follows:

$$\mathbf{X}^{(k+1)} = \eta_{q,\lambda\mu}\left(\mathbf{X}^{(k)} + \mu\mathcal{I}\left(\mathbf{Y} - \sum \mathcal{G}_j\left(\mathbf{X}^{(k)}\right)\right)\right) \quad (8)$$

where $\mathcal{I}(\cdot)$ represents the multichannel SAR imaging operator [19], which consists of Doppler spectrum reconstruction, range compression, range cell migration correction (RCMC), and azimuth-matched filtering.

The details of the L_q-regularization-based multichannel SAR imaging method is shown in [19]. For the nonuniform sampling case, where the PRF of each channel is greater than the uniform PRF or the phase center of receiving antenna deviates from the ideal sampling position, this method can reduce the noise and suppress the resulting azimuth ambiguities. However, for the nonuniform undersampling case mentioned in this article, the abovementioned model is no longer applicable. We will address this issue in the following sections.

III. $L_{2,q}$-Regularization-Based Multichannel SAR Imaging Method for Nonuniform Undersampling

In this section, we will first analyze the factors of azimuth ambiguities in the nonuniform undersampling case of the multichannel SAR system. Then, the novel sparse SAR imaging model of nonuniform undersampling is established, and the multichannel SAR data processing operators are introduced into the $L_{2,q}$-regularization-based solution formula. Finally, the sparse group threshold iteration algorithm is adopted to recover the scene of interest.

A. Azimuth Ambiguities in the Nonuniform Undersampling Multichannel SAR System

As stated in [10] and [11], for a multichannel SAR system with M channels, if each channel is undersampled at $1/M$ of the original signal's Nyquist frequency, the Doppler spectrum of the original signal can be reconstructed unambiguously from the aliased spectrums of these M independent signals. Let PRF denote the PRF of each channel. The derivation of the Doppler spectrum reconstruction can be found in Appendix A.

The next discussion is based on $M = 2$. The reconstruction filter matrix actually represents a linear system, which can recover the original spectrum while cancelling the aliased components caused by the folded spectra. However, for the case when signal bandwidth exceeds $M \cdot \mathrm{PRF}$, the sampling scheme no longer satisfies the Nyquist criterion, boiling down to the nonuniform undersampling scheme. In this case, it can be observed that for each frequency, the spectra of the subsampled signal $U_{j,p}(f)$ are composed of up to three components, as shown in the top of Fig. 2(a). This means that more than two spectra may overlap at a specific Doppler frequency [12].

For the dual-channel nonuniform undersampling case, the factors of azimuth ambiguities can be divided into two aspects, as shown in Fig. 2(a). First, due to undersampling, the subsampled signal $U_{j,p}(f)$ consists of more than two overlapped spectra. This will result in the linear system containing the bandpass reconstruction filters to be underdetermined [12]. Therefore, the original spectrum cannot be reconstructed exactly due to the mismatch of reconstruction filters at the ± 1 st ambiguous areas e_{-1} and e_1. Second, after Doppler spectrum reconstruction, the equivalent azimuth sampling rate $M \cdot \mathrm{PRF}$ will be less than the Doppler bandwidth of the original signal, which also leads to aliasing in Doppler spectrum at the $\pm 2\mathrm{nd}$ ambiguous areas e_{-2} and e_2. Fig. 2(b) is the diagram of azimuth ambiguities in dual-channel SAR geometry, where $\mathbf{x}_0$

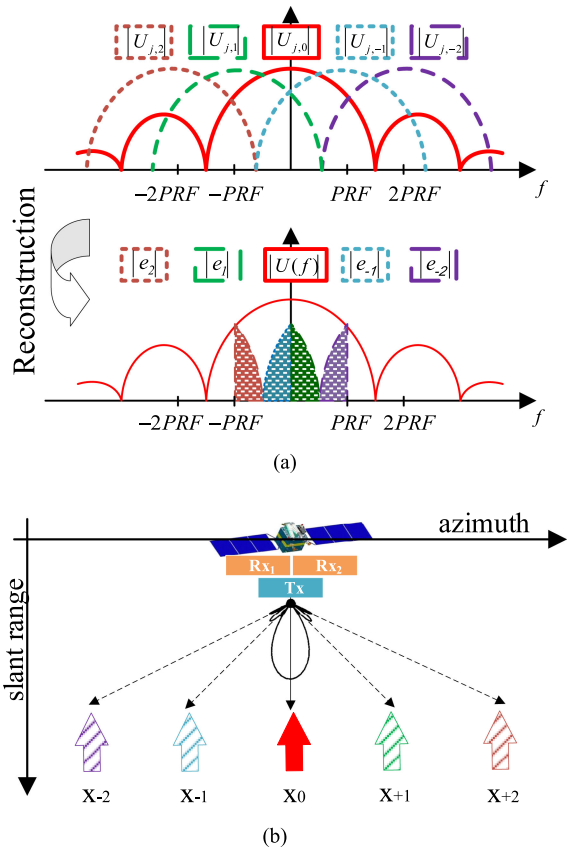

Fig. 2. Illustration of azimuth ambiguities for dual-channel nonuniform undersampling scheme. (a) Causes of azimuth ambiguities in dual-channel SAR system. (b) Diagram of azimuth ambiguities in dual-channel SAR geometry.

denotes the main imaging area, $\mathbf{x}_i (i = -2, -1, +1, +2)$ denote the ± 1st and ± 2nd ambiguous areas, respectively.

B. Sparse SAR Imaging Model in Multichannel System

As discussed above, due to the nonuniform undersampling, the azimuth ambiguous areas in the dual-channel system consist of four parts. In contrast in the undersampled single-channel SAR system, only the ± 1st ambiguous areas are considered because there is no Doppler spectrum reconstruction process [21]. Hence, we cannot directly adopt its imaging model. Combining all the ambiguous areas and the main imaging area together, the dual-channel sparse SAR imaging model containing azimuth ambiguities can be expressed as follows:

$$\mathbf{y} = [\mathbf{\Phi}_{-2}\ \mathbf{\Phi}_{-1}\ \mathbf{\Phi}_0\ \mathbf{\Phi}_{+1}\ \mathbf{\Phi}_{+2}]\,[\mathbf{x}_{-2}\ \mathbf{x}_{-1}\ \mathbf{x}_0\ \mathbf{x}_{+1}\ \mathbf{x}_{+2}]^{\mathrm{T}} + \mathbf{n} = \mathbf{\Phi}\mathbf{x} + \mathbf{n} \tag{9}$$

where $\mathbf{\Phi} = [\mathbf{\Phi}_{-2}\ \mathbf{\Phi}_{-1}\ \mathbf{\Phi}_0\ \mathbf{\Phi}_{+1}\ \mathbf{\Phi}_{+2}]$; $\mathbf{x} = [\mathbf{x}_{-2}\ \mathbf{x}_{-1}\mathbf{x}_0\ \mathbf{x}_{+1}\ \mathbf{x}_{+2}]^{\mathrm{T}}$; $\mathbf{x}_0 \in \mathbb{C}^{N\times 1}$ is the unambiguous image of the main imaging area; $\mathbf{x}_{-2} \in \mathbb{C}^{N\times 1}$ and $\mathbf{x}_{+2} \in \mathbb{C}^{N\times 1}$ are the images of ± 2nd ambiguous area, respectively; $\mathbf{x}_{-1} \in \mathbb{C}^{N\times 1}$ and $\mathbf{x}_{+1} \in \mathbb{C}^{N\times 1}$ are the images of ± 1st ambiguous area, respectively; $\mathbf{n} \in \mathbb{C}^{N\times 1}$ is the noise vector; $\mathbf{\Phi}_i = [\phi_i^1, \ldots, \phi_i^M]\,(i = -2, -1, 0, +1, +2)$, and $\phi_i^j \triangleq \{\phi_i^j(m,n)\}$ are the observation matrices of the jth $(j = 1, 2)$ channel of the main imaging area $(i = 0)$ and the ± 1 st and ± 2nd $(i = -2, -1, +1, +2)$ ambiguous areas, respectively. The observation matrices ϕ_i^j represent the mapping relationship from the backscattered coefficient of the observed scene to the echo data, whose elements can be represented as follows:

$$\begin{aligned}\phi_i^j\ (m,n) &= \omega_a\ \left(t_m - \frac{p_n}{v}\right) \\ &\cdot \exp\left\{-j2\pi \frac{R\,(p_n, q_n, t_m) + R_j\,(p_n, q_n, t_m)}{\lambda}\right\} \\ &\cdot\ s\left(\tau_m - \frac{R\,(p_n, q_n, t_m) + R_j\,(p_n, q_n, t_m)}{c}\right) \\ &\cdot \exp\{j \cdot i\mathrm{PRF} \cdot t_m\}\end{aligned} \tag{10}$$

where $s\ (\tau) = \exp\{j\pi K_r \tau^2\}$ is the transmitted chirp signal with the chirp rate K_r; $R(p,q,t) = \sqrt{{R_{q,0}}^2 + (vt - x_p)^2}$ is the instantaneous distance from the transmitter to the target, $R_{q,0}$ is the minimum slant distance of the q–t range cell, x_p is the pth azimuth position; $R_j(p,q,t)$ is the distance from the jth receiver to the target, with $R_j(p,q,t) = R(p,q,t - \Delta x_j/v)$, and Δx_j is the distance between the transmitter and the jth receiver; $\omega_a(t)$ is the two-way antenna pattern. Considering the actual SAR signal is not band-limited, $\omega_a(t)$ can be expressed as follows:

$$\omega_a\ (t) = \mathrm{sinc}^2\left(\frac{D}{\lambda}\theta\,(t)\right) \tag{11}$$

where D is the aperture of transmitting antenna and θ is the squint angle along the slant-range plane.

Next, we study the solution of the sparse SAR imaging model (9). Although the amplitude and phase of the elements in $\mathbf{x}_i (i = -2, -1, 0, +1, +2)$ are different, they share the same sparse support set [20]. Taking the elements at the same position in $\mathbf{x}_i$ as a group, their coefficients will be zero or nonzero at the same time, as shown in Fig. 3, where the intragroup elements are shown in the same color but different line types, and the intergroup elements are plotted by the same line type but different colors. This particular structural property is called the group sparsity constraint.

The group sparsity constraint has been applied into the single-channel SAR imaging to improve sparse recovery performance already [21], [24], and we can extend it into the multichannel SAR system. We solve (9) by utilizing the sparse group LASSO model [25]

$$\hat{\mathbf{x}} = \underset{\mathbf{x}}{\mathrm{argmin}}\ \left\{\|\mathbf{y} - \mathbf{\Phi}\mathbf{x}\|_2^2 + \lambda_1 \|\mathbf{x}\|_{2,q}^q + \lambda_2 \|\mathbf{x}\|_1\right\} \tag{12}$$

where the first penalty term is 2, q-norm term; the second penalty term is 1-norm term, which is used to constrain the sparsity of the main imaging area and suppress the residual ambiguous energy; λ_1 and λ_2 are the regularization parameter of the 2, q-norm term and the 1-norm term, respectively. In model (12), the 2, q-norm term reflects the group sparsity property of the main imaging

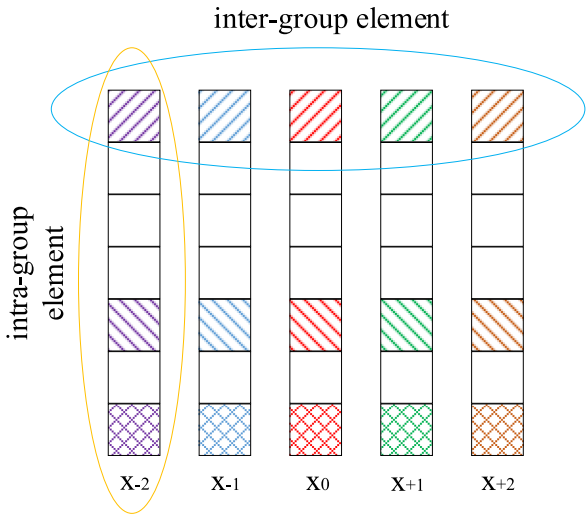

Fig. 3. Group sparsity constraint in nonuniform undersampling dual-channel system, where imaging area and ambiguous areas $\mathbf{x}_i (i = -2, -1, 0, +1, +2)$ share the same sparse support.

area and ambiguous areas, which is defined as follows:

$$\|\mathbf{x}\|_{2,q}^{q} = \left(\sum_{n=1}^{N} \left(\sum_{i} |\mathbf{x}_i (n)| \right)^{q} \right)^{\frac{1}{q}}. \tag{13}$$

By solving the $L_{2,q}$ regularization problem (12), the azimuth ambiguities in the nonuniform undersampled dual-channel SAR system can be suppressed effectively.

C. Multichannel SAR Data Processing Operators

As discussed above, the observation-matrix-based sparse SAR imaging method vectorizes the echo data matrix, incurring azimuth-range coupling, hence, huge computational costs. Its computational complexity is proportional to the quadratic square of the scene size. Besides, the dual-channel sparse SAR imaging model (9) consists of five observation matrices, quintupling the problem scale. Therefore, solving (12) directly would involve tremendous computation complexity and cannot be applied toward large-scale scene.

Inspired by [17], according to the idea of approximated observation, we introduce the multichannel SAR data processing operators into the $L_{2,q}$ regularization to replace the matrix–vector multiplication operation, reducing the problem scale and computational complexity. Different from the L_q-regularization-based reconstruction method presented in Section II, not only the processing operators of the main imaging area, but also the processing operators of ambiguous areas are considered.

Let $\mathcal{I}_i(\cdot)$ with $i = 0$ and $i \in \mathbb{Z},\ i \neq 0$ denote the multichannel SAR imaging operators of the main imaging area and ambiguous areas, respectively. In [10], a Doppler spectrum reconstruction method based on generalized sampling theorem has been proposed. The signal acquisition of the multichannel SAR system can be expressed as a monostatic SAR response passing a transfer filters system. As shown in Appendix A, the Doppler spectrum can be reconstructed using a set of functions determined by those filters. Therefore, the multichannel SAR imaging consists of two steps, Doppler spectrum reconstruction and monostatic SAR imaging.

In this article, the filter bank method in [10] is chosen as the Doppler spectrum reconstruction method, and the chirp scaling algorithm (CSA) [26] is chosen as the monostatic SAR imaging method. It should be noticed that the composition of the multichannel SAR imaging operators in the ambiguous areas are similar to that in the main imaging area, except that the azimuth frequencies are different:

$$f_{a,i} = f_{a,0} + i \cdot \mathrm{PRF},\ i \in \mathbb{Z} \tag{14}$$

where $f_{a,0}$ is the azimuth frequency of the Doppler spectrum in the main imaging area, and $f_{a,i}$ are the azimuth frequencies of the Doppler spectrum in ambiguous areas ($i \neq 0$). Then the multichannel SAR imaging operators of the main imaging area ($i = 0$) and ambiguous areas ($i \neq 0$) can be written as follows:

$$\begin{aligned} \mathcal{I}_i\ (\mathbf{Y}) = \boldsymbol{F}_a^{-1} \\ \{\boldsymbol{\Theta}_i^{ac} \odot \{\boldsymbol{\Theta}_i^{rc} \odot \{\boldsymbol{\Theta}_i^{sc} \odot [\sum_{j=1}^{M} \mathbf{P}_i^j \odot \boldsymbol{F}_a(\mathbf{Y}_j)] \\ \boldsymbol{F}_r\} \boldsymbol{F}_r^{-1}\}\} \end{aligned} \tag{15}$$

where $\mathbf{Y}_j$ is the two-dimensional (2-D) echo data of the jth ($j = 1, 2$) channel; $\boldsymbol{F}_a$ and $\boldsymbol{F}_r$ are the Fourier transform (FFT) operators in azimuth and range; $\boldsymbol{F}_a^{-1}$ and $\boldsymbol{F}_r^{-1}$ are the corresponding inverse Fourier transform (IFFT) operators, and $\odot$ denotes the Hadamard product. The detailed explanations and derivations of (15) are given in Appendix B.

The echo data generation procedure is actually the inverse of the imaging procedure. Hence, considering the procedure of the multichannel SAR imaging, the multichannel SAR echo data generation operators of the jth channel of the main imaging area ($i = 0$) and ambiguous areas ($i \neq 0$) can be written as follows:

$$\begin{aligned} \mathcal{G}_i^j\ (\mathbf{X}_i) = \boldsymbol{F}_a^{-1} \{(\mathbf{P}_i^j)^* \odot \{\boldsymbol{\Theta}_i^{sc*} \odot \{\boldsymbol{\Theta}_i^{rc*} \odot \{\boldsymbol{\Theta}_i^{ac*} \odot \\ [\boldsymbol{F}_a\,(\mathbf{X}_i)]\, \boldsymbol{F}_r\} \boldsymbol{F}_r^{-1}\}\}\} \end{aligned} \tag{16}$$

where $\mathbf{X}_i \in \mathbb{C}^{N_a \times N_r}$ are the 2-D backscattered coefficient matrices of different areas and $(\cdot)^*$ is the conjugate transpose operation. Due to the Doppler spectrum reconstruction, both $\mathcal{I}_i(\cdot)$ and $\mathcal{G}_i^j(\cdot)$ are different from those in single-channel SAR systems.

After constructing the multichannel SAR data processing operators of the main imaging area and ambiguous areas, we can rewrite the nonuniform undersampling dual-channel sparse SAR imaging model (9) by replacing the observation matrices $\boldsymbol{\Phi}$ with $\mathcal{G}_i^j(\cdot)$

$$\mathbf{Y}_j = \sum_{i} \mathcal{G}_i^j\,(\mathbf{X}_i) + \mathbf{N}_j, \tag{17}$$

where $\mathbf{N}_j \in \mathbb{C}^{N_a \times N_r}$ is the noise matrix of the jth ($j = 1, 2$) channel. Then, we can reconstruct the considered scene by solving the modified $L_{2,q}$ regularization problem using the

multichannel SAR data processing operators:

$$\hat{\mathbf{X}} = \underset{\mathbf{X}}{\operatorname{argmin}} \left\{ \| \cup_j \mathbf{Y}_j - \sum_i \mathcal{G}_i^j (\mathbf{X}_i) \|_2^2 + \lambda_1 \|\mathbf{X}\|_{2,q}^q + \lambda_2 \|\mathbf{X}\|_1 \right\} \quad (18)$$

where $\mathbf{X} = [\mathbf{X}_{-2}, \mathbf{X}_{-1}, \mathbf{X}_0, \mathbf{X}_{+1}, \mathbf{X}_{+2}]$; and $\mathbf{X}_0$ is the recovered sparse SAR imagery. Compared with (12), the problem scale of (18) is reduced remarkedly by decoupling the range and azimuth operations.

D. Sparse Group Threshold Iteration

According to [25] and [27], the sparse group LASSO model in (18) can be solved by sparse group iteration algorithm. In this article, we choose $q = 1$ as an example to verify the effectiveness of the proposed multichannel SAR imaging method for nonuniform undersampling. The kth iteration formula can be represented as follows:

$$\begin{aligned} \mathbf{X}^{(k+1)} &= \underset{\mathbf{X}}{\operatorname{argmin}} \left\{ \sum_i \left\| \boldsymbol{X}_i{}^{(k)} - \overline{\mathbf{U}}_i{}^{(k)} \right\|_2^2 + \lambda_1 \|\mathbf{X}\|_{2,1}^1 + \lambda_2 \|\mathbf{X}\|_1 \right\} \\ &= H_{2|1,\lambda_1\mu} \left(\left[\overline{\mathbf{U}}_{-2}{}^{(k)}, \overline{\mathbf{U}}_{-1}{}^{(k)}, \overline{\mathbf{U}}_0{}^{(k)}, \overline{\mathbf{U}}_{+1}{}^{(k)}, \overline{\mathbf{U}}_{+2}{}^{(k)} \right] \right) \end{aligned} \quad (19)$$

where μ is the step size parameter controlling the convergence speed of the iteration algorithm, and $H_{2|1,\lambda_1\mu}(\cdot)$ is the sparse group thresholding function

$$\begin{aligned} &H_{2|1,\lambda_1\mu} \left(\left[\overline{\mathbf{U}}_{-2}{}^{(k)}, \overline{\mathbf{U}}_{-1}{}^{(k)}, \overline{\mathbf{U}}_0{}^{(k)}, \overline{\mathbf{U}}_{+1}{}^{(k)}, \overline{\mathbf{U}}_{+2}{}^{(k)} \right] \right) \\ &= \left[\overline{\mathbf{U}}_{-2}{}^{(k)}, \overline{\mathbf{U}}_{-1}{}^{(k)}, \overline{\mathbf{U}}_0{}^{(k)}, \overline{\mathbf{U}}_{+1}{}^{(k)}, \overline{\mathbf{U}}_{+2}{}^{(k)} \right] \\ &\quad \cdot \max \left(1 - \frac{\lambda_1 \mu}{\left\| \mathbf{U}_g{}^{(k)} \right\|_2}, 0 \right). \end{aligned} \quad (20)$$

Within the solution of the sparse group LASSO model (18), the sparse group threshold iteration guarantees the sparsity constraints between the main imaging area and ambiguous areas, and the soft thresholding operation in each area can further remove the residual ambiguous energy, improving the performance of azimuth ambiguities suppression.

Table I summarizes the iterative procedures of the proposed $L_{2,1}$-regularization-based multichannel SAR imaging method for nonuniform undersampling. For other q values ($q < 1$), such as $q = 1/2$ and $q = 2/3$, the corresponding iterative procedures are identical to Table I except for the sparse group thresholding function $H_{2|q,\lambda_1\mu}(\cdot)$, which can be derived from [28]. In Table I, K is the sparsity of the considered scene; $\|\cdot\|_F$ is the Frobenius norm and $\eta_{1|\lambda_2\mu}(\cdot)$ is the soft thresholding

TABLE I
MULTICHANNEL SAR IMAGING FOR NONUNIFORM UNDERSAMPLING BASED ON $L_{2,q}$ REGULARIZATION ($q = 1$)

Input:

Nonuniform under-sampling multichannel SAR echo data $\mathbf{Y}$;

Multichannel SAR data processing operators $\mathcal{I}_i(\cdot)$ and $\mathcal{G}_i^j(\cdot)$ ($i = -2, -1, 0, +1, +2$ $j = 1, 2$)

Initialization:

$\mathbf{X}_i{}^{(0)} = 0$; $\mathbf{U}_i{}^{(0)} = 0$; $\mathbf{U}_g{}^{(0)} = \mathbf{U}_0{}^{(0)}$; $k = 0$

Step parameter μ;

Error parameter ε;

Maximum iteration steps k_{max}

Sparsity K;

while $Reli > \varepsilon$ and $k < k_{max}$

1. Estimate the residual:

$$\Delta^{(k+1)} = \cup_j \mathbf{Y}_j - \textstyle\sum_i \mathcal{G}_i^j \left(\mathbf{X}_i{}^{(k)} \right)$$

2. Update the gradient direction:

$$\mathbf{U}_i{}^{(k+1)} = \mathbf{X}_i{}^{(k)} + \mu \mathcal{I}_i \left(\Delta^{(k+1)} \right)$$

3. Update the regularization parameter of 1-norm term:

$$\lambda_2 = \left| \mathbf{U}_0{}^{(k+1)} \right|_{K+1} / \mu$$

4. Soft thresholding for imaging area and ambiguous areas:

$$\bar{\mathbf{U}}_i{}^{(k+1)} = \eta_{1|\lambda_2\mu} \left(\mathbf{U}_i{}^{(k+1)} \right)$$

5. Update the group imaging area:

$$\mathbf{U}_g{}^{(k+1)} = \sqrt{\textstyle\sum_{i=-2}^{2} \left| \left(\bar{\mathbf{U}}_i{}^{(k+1)} \right) \right|^2}$$

6. Update the regularization parameter of 2, 1-norm term:

$$\lambda_1 = \left| \mathbf{U}_g{}^{(k+1)} \right|_{K+1} / \mu$$

7. Sparse Group Threshold Iteration:

$$\begin{aligned} &[\mathbf{X}_{-2}{}^{(k+1)}, \mathbf{X}_{-1}{}^{(k+1)}, \mathbf{X}_0{}^{(k+1)}, \mathbf{X}_{+1}{}^{(k+1)}, \mathbf{X}_{+2}{}^{(k+1)}] \\ &= H_{2|1,\lambda_1\mu} \left([\bar{\mathbf{U}}_{-2}{}^{(k+1)}, \bar{\mathbf{U}}_{-1}{}^{(k+1)}, \bar{\mathbf{U}}_0{}^{(k+1)}, \bar{\mathbf{U}}_{+1}{}^{(k+1)}, \bar{\mathbf{U}}_{+2}{}^{(k+1)}] \right) \end{aligned}$$

8. Calculate the iteration error:

$$Reli = \left\| \mathbf{X}_0{}^{(k+1)} - \mathbf{X}_0{}^{(k)} \right\|_F$$

9. Update the iteration step:

$$k = k + 1$$

end while

Output:

The recovered image $\mathbf{X}_0{}^{(k)}$

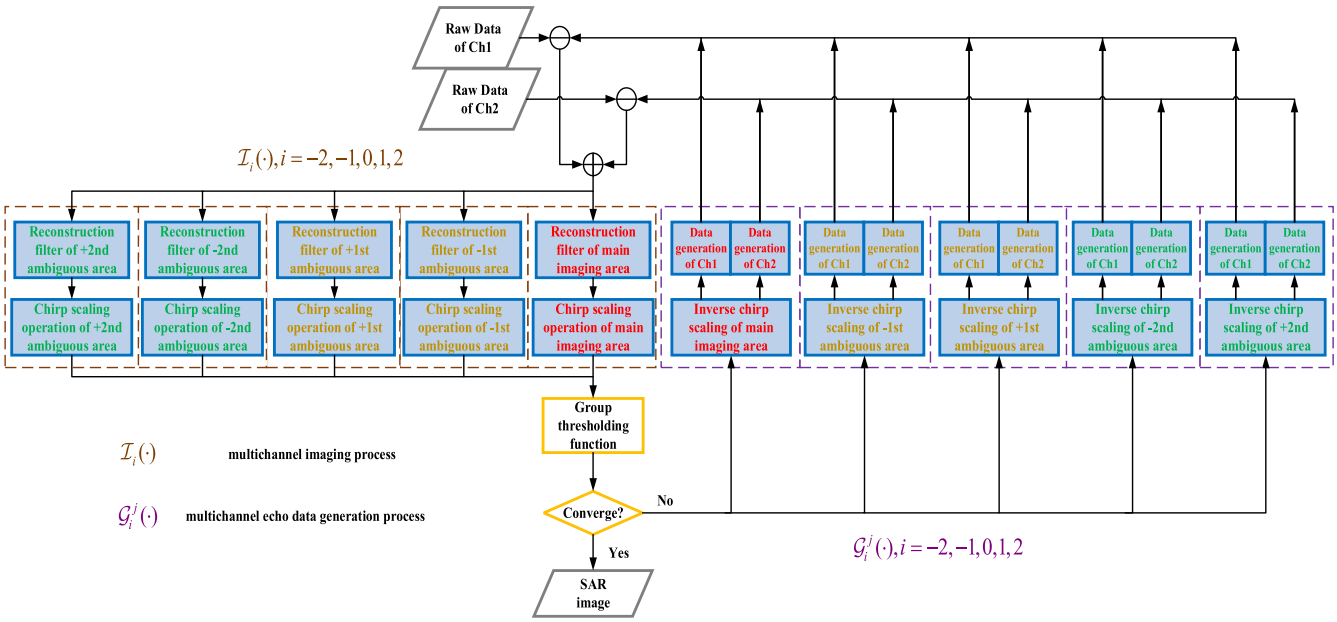

Fig. 4. Flowchart of the proposed $L_{2,q}$-regularization-based dual-channel SAR imaging method.

function

$$\eta_{1|\lambda_2\mu}(x)=\begin{cases} sign(x)\left(|x|-\lambda_2\mu\right), & |x|\geq\lambda_2\mu \\ 0, & |x|<\lambda_2\mu \end{cases} \tag{21}$$

where $\mathrm{sign}(\cdot)$ is the sign function and the threshold $\lambda_2\mu$ is determined by the $(K+1)$th largest element of the amplitude of $|\mathbf{U}_0{}^{(k+1)}|$.

Compared with the L_q-regularization-based multichannel SAR imaging method, the proposed method takes the ambiguous areas into account when constructing the sparse SAR imaging model. The flowchart of the proposed method is shown in Fig. 4.

IV. Simulation and Gaofen-3 Data Experiments

In this section, both simulations and Gaofen-3 real data experiments have been carried out to validate the effectiveness of the proposed method.

A. Numerical Simulations

In this part, the numerical simulations will be exploited using the parameters of the Gaofen-3 dual-channel mode. In order to show the azimuth ambiguities caused by the nonuniform undersampling better, the simulation data are generated without channel imbalance. The major parameters in simulation experiments are listed in Table II.

According to the platform velocity and antenna aperture in Table II, it can be calculated that the PRF satisfying uniform sampling is 2013.63 Hz. In order to generate the nonuniform undersampled data, the PRF of each channel is set to 1610.91 Hz at 80% undersampling. The 2-D simulations are presented in the first experiment. The imaging results of the proposed $L_{2,1}$-regularization-based method are shown in Fig. 5 with benchmarks of spectrum reconstruction algorithm (SRA) in [10] and

Table II
Major Parameters in Simulation Experiments

Parameters	Value
Platform velocity	7551.119147 m/s
Wavelength	0.055517 m
Sampling rate	133.33 MHz
Bandwidth	100 MHz
Pulse duration	55 μs
Center slant range	918 km
Pulse repetition frequency (PRF)	1610.91 Hz
Antenna aperture	3.75 m

L_1-regularization-based method in [19]. The specific analysis is as follows.

Fig. 5 shows the reconstructed 2-D images of one-point target with three aforementioned methods. The point target is located in the center of the scene. White additive noise with different SNRs (20 and 10 dB) are added to the simulated data to demonstrate the ambiguities suppression effects of different methods better. The corresponding reconstructed images are shown in the top row and bottom row in Fig. 5, respectively.

The imaging results of SRA under different SNRs are shown in Fig. 5(a) and (d). It is obvious that due to nonuniform undersampling, the SRA cannot recover the scene of interest accurately and the azimuth ambiguities appears in the ± 1 st and ± 2nd ambiguous areas, which is consistent to the theoretical analysis mentioned above. Besides, due to the existence of range cell migration, the azimuth ambiguities in the 2-D image domain are not located in the same range cell any longer, which will be analyzed in the following paragraph.

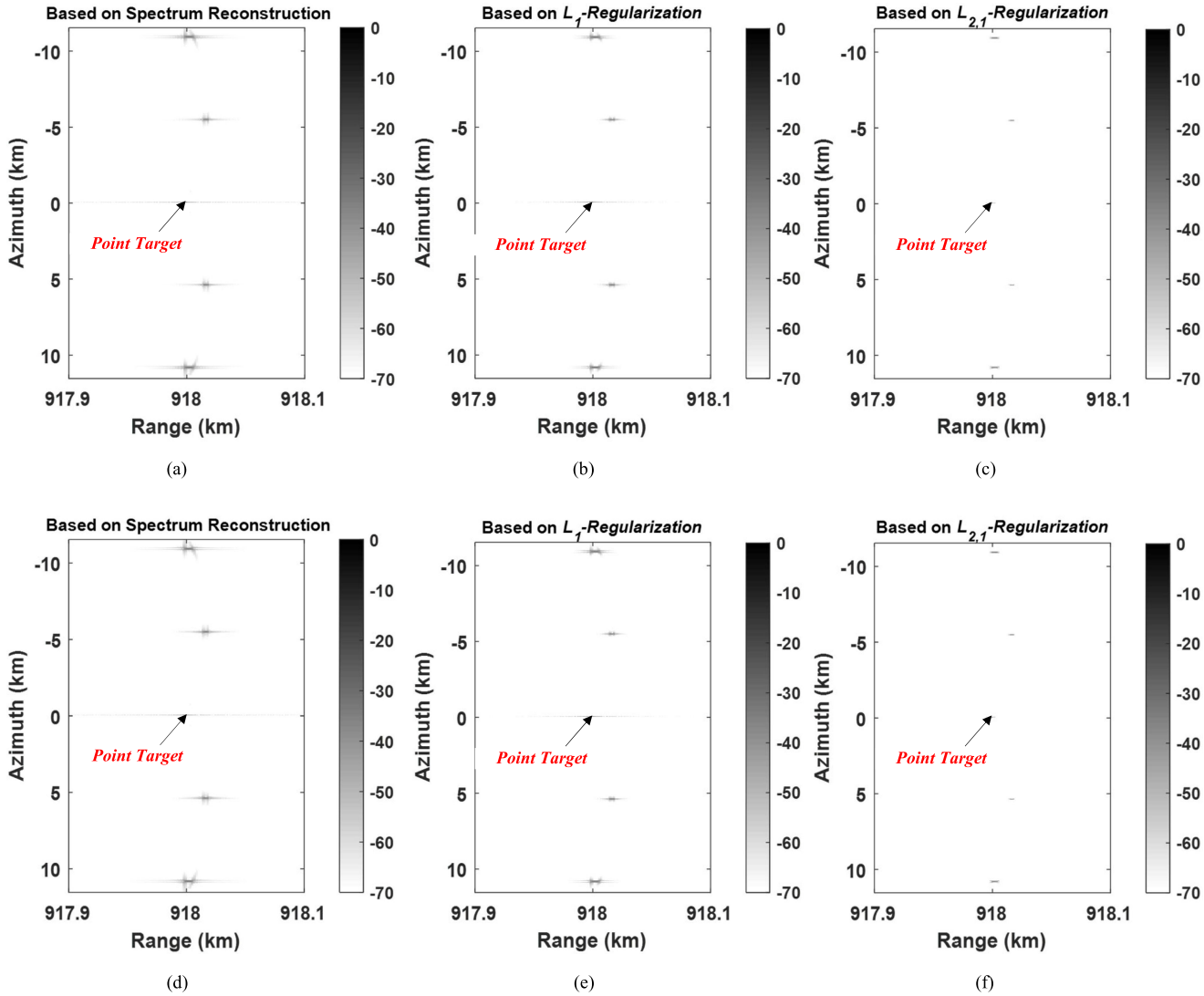

Fig. 5. 2-D reconstructed images of the point target in nonuniform undersampling dual-channel system by SRA in [10], L_1-regularization-based method in [19] and $L_{2,1}$-regularization-based method under different SNR. Top: SNR $=$ 20 dB. Bottom: SNR $=$ 10 dB. (a) and (d) SRA. (b) and (e) L_1-regularization. (c) and (f) $L_{2,1}$-regularization. (undersampling rate is 80%.).

Let $\widetilde{\mathrm{PRF}}$ denote the azimuth sampling rate after the Doppler spectrum reconstruction process, $\widetilde{\mathrm{PRF}} = 2\mathrm{PRF}$. The azimuth frequency in the main imaging area can be expressed as $f_{a,0} \in (-\widetilde{\mathrm{PRF}}/2, \widetilde{\mathrm{PRF}}/2]$. As analyzed in Section III, the mismatch of reconstruction filters causes the $\pm 1\mathrm{st}$ ambiguous areas and the undersampling causes the $\pm 2\mathrm{nd}$ ambiguous areas. Their corresponding azimuth frequencies can be expressed as $f_{a,i} = f_{a,0} + i \cdot \mathrm{PRF}$ $(i = -2, -1, +1, +2)$, as shown in (14). The operation $\mathbf{\Theta}_i^{rc}(f_{a,i})$ $(i = 0)$ in CSA can achieve the RCMC of the main imaging area. However, for the ambiguous areas, the curvature of range profiles in the Doppler domain is different from that in the main imaging area, and the RCMC operations of ambiguous areas $\mathbf{\Theta}_i^{rc}(f_{a,i})$ $(i \neq 0)$ are mismatched with the main imaging area. Hence, the range cell of $\pm 1\mathrm{st}$ and $\pm 2\mathrm{nd}$ ambiguous areas will deviate from that of the main imaging area, as shown in Fig. 5(a) and (d).

The reconstructed 2-D images of the L_1-regularization-based method under different SNRs are shown in Fig. 5(b) and (e). It can be seen that this method can suppress the noise and sidelobes effectively. However, it does not have the ability to suppress azimuth ambiguities for the $\pm 1\mathrm{st}$ and $\pm 2\mathrm{nd}$ ambiguous areas. As a contrast, the reconstructed 2-D images of the proposed $L_{2,1}$- regularization-based method are shown in Fig. 5(c) and (f). Compared with the L_1-regularization-based method, the proposed $L_{2,1}$-regularization-based method takes the components of different ambiguous areas into account when constructing the imaging model. Therefore, the proposed method cannot only reduce the noise component, but also achieve ambiguities suppression in the azimuth multichannel SAR system for nonuniform undersampling, which can be observed from the imaging results in Fig. 5. It can also be concluded from Fig. 5 that the $L_{2,1}$-regularization-based method can achieve the similar ambiguity suppression effectiveness under different SNRs, which is robust to the noise.

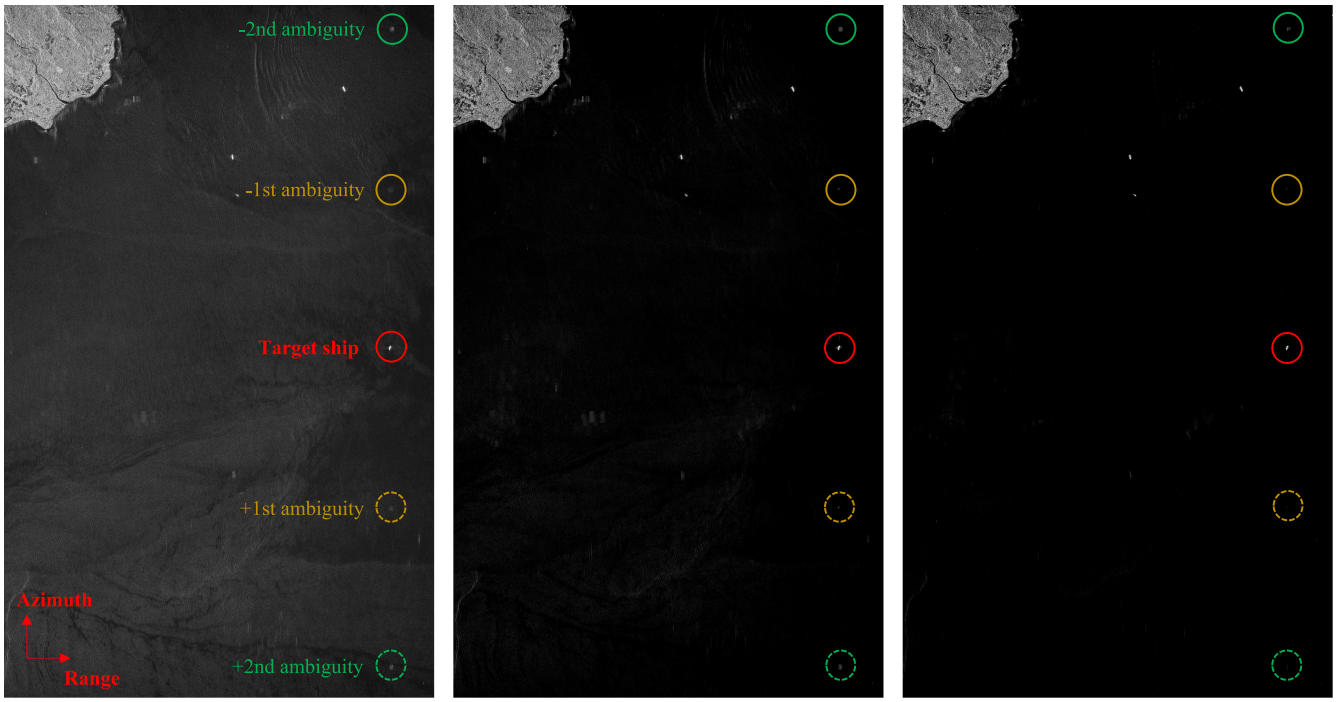

Fig. 6. Reconstructed images of the observed scene. (a) Gaofen-3 dual-channel mode product. (b) L_1-regularization-based method in [19]. (c) $L_{2,1}$-regularization-based method. The azimuth and range directions are marked in (a).

In order to quantitatively evaluate the azimuth ambiguities suppression ability of the $L_{2,1}$-regularization-based method, we select the azimuth ambiguity-to-signal ratio (AASR) as the evaluation indicator in this article, and the AASR value of the i-th ambiguous area is defined as

$$\mathrm{AASR}_i = 10\log_{10}\left(\frac{\frac{1}{N_G}\sum_{(p,q)\in M_i}\left|\mathbf{X}_{(p,q)}\right|^2}{\frac{1}{N_A}\sum_{(p,q)\in\mathcal{A}}\left|\mathbf{X}_{(p,q)}\right|^2}\right) \tag{22}$$

where $\mathcal{A}$ is the main imaging area, N_A is the numbers of the pixel in $\mathcal{A}$, M_i is the ith ambiguous area, and N_G is the numbers of the pixel in M_i.

To further analyze the imaging performance of SRA in [10], the L_1-regularization-based method in [19] and the proposed $L_{2,1}$-regularization-based method, the AASR values of different ambiguous areas need to be compared. Therefore, in the second simulation experiment, the AASR values of the 1 st ambiguous area and the 2nd ambiguous area with the different undersampling rate are calculated, where the azimuth antenna pattern is chosen as (11) and the SNR is set to 20 dB. The experimental results of the different undersampling rate are summarized in Table III.

From Table III, it can be seen that compared with SRA in [10], the L_1-regularization-based method in [19] can only reduce the AASR values by about 2 dB. In contrast, for the different undersampling rate, the $L_{2,1}$-regularization-based method can reduce the AASR values of both $\pm$1st and $\pm$2nd ambiguous areas by more than 10 dB, which proves the effectiveness of the ambiguity suppression ability under the nonuniform undersampling case.

TABLE III
AASR VALUES WITH DIFFERENT UNDERSAMPLING RATE [DB]

under-sampling rate	AASR_{-1}			AASR_{-2}		
	SRA	L_1	$L_{2,1}$	SRA	L_1	$L_{2,1}$
75%	-16.57	-17.52	-27.47	-13.62	-15.03	-23.86
80%	-19.29	-20.64	-33.54	-15.32	-16.41	-25.75
85%	-23.71	-25.65	-38.09	-17.18	-19.24	-28.13
90%	-27.33	-30.05	-43.28	-19.67	-21.45	-31.49

B. Gaofen-3 Dual-Channel Data Processing

Gaofen-3 is a Chinese spaceborne satellite for scientific applications carrying a *C*-band SAR sensor, which was launched in August 2016, from Taiyuan (Shanxi Province, China). It has provided customers with advanced spaceborne SAR products since January 2017.

Gaofen-3 is also the first Chinese spaceborne azimuth multichannel SAR containing two receiving antennas along the azimuth, and can obtain images with azimuth resolution of 3 m and swath width of 30 km in the ultra-fine stripmap (UF) mode, i.e., the dual-channel mode [9]. To further show the influence of nonuniform undersampling scheme in the multichannel SAR system and explore the validity of the $L_{2,1}$- regularization-based method for ambiguities suppression, Gaofen-3 dual-channel data are processed in this part. The PRF of each channel in

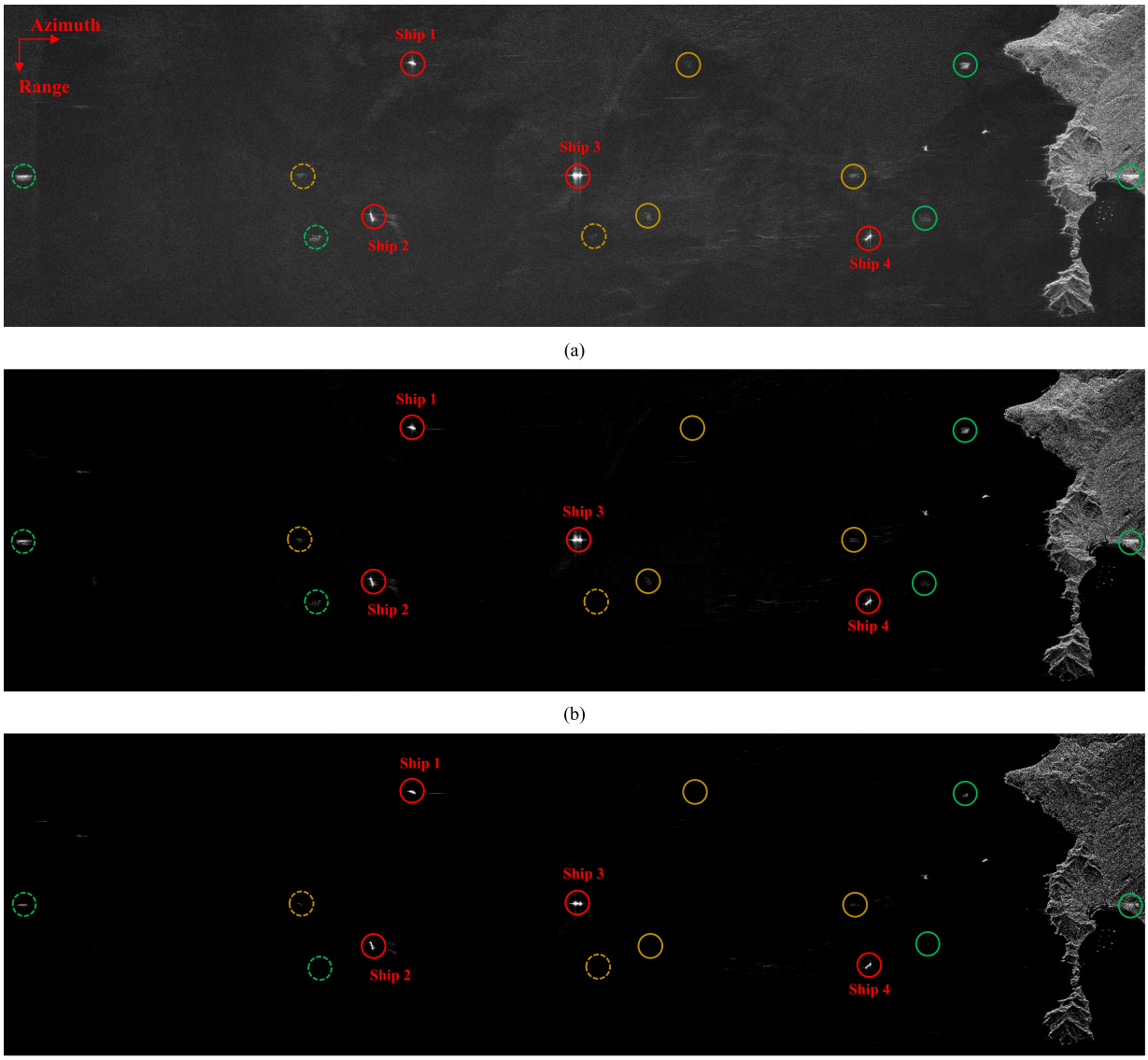

Fig. 7. Imaging results of the Gaofen-3 dual-channel data by different methods. (Nonuniform undersampling scheme) (a) SRA in [10]. (b) L_1-regularization-based method in [19]. (c) $L_{2,1}$,-regularization-based method. The $+1$st and $+2$-nd ambiguous areas of Ship 1 and Ship 2 are not marked due to their weak ambiguous energy.

the experimental data are 1976.93 Hz. The other parameters are identical to that in Table II.

In the first experiment, we compare the imaging results of the L_1-regularization-based method and $L_{2,1}$- regularization-based method with the original product image without any special processing, as shown in Fig. 6. It can be seen that compared with the product image, both the L_1-regularization-based method and $L_{2,1}$- regularization-based method can suppress the background noise on the sea surface. To quantitatively evaluate the noise suppression effect, we select one ship denoted by the red circle as the observed target, and the target-to-background ratio (TBR) [29] is selected as the evaluation criterion, which is defined as follows:

$$\mathrm{TBR}\ (\mathbf{X}) = 20\log_{10}\left(\frac{\max_{(p,q)\in T}\left|\boldsymbol{X}_{(p,q)}\right|}{\frac{1}{N_B}\sum_{(p,q)\in B}\left|\boldsymbol{X}_{(p,q)}\right|}\right) \tag{23}$$

where T is the target region, B is the background area, and N_B is the numbers of the pixel in B.

The TBR value of the ship in the product image Fig. 6(a) is 24.26 dB, and the TBR values of the target ship in the images of the L_1-regularization-based method Fig. 6(b) and the $L_{2,1}$- regularization-based method Fig. 6(c) are 40.57 dB and 41.18 dB, respectively. It can be concluded that these two methods have the similar noise reducing performance. However, they perform differently on the suppression of azimuth ambiguities. From the product image Fig. 6(a), we can see that due to nonuniform undersampling, the target has ± 1st and ± 2nd ambiguous areas, marked by brown circles and green circles, which is consistent with the analysis in Section III. The AASR values of 1st ambiguous areas AASR_{-1} and 2nd ambiguous area AASR_{-2} are –34.54 and –22.04 dB, respectively. In the reconstructed image of the L_1-regularization-based method Fig. 6(b), AASR_{-1}

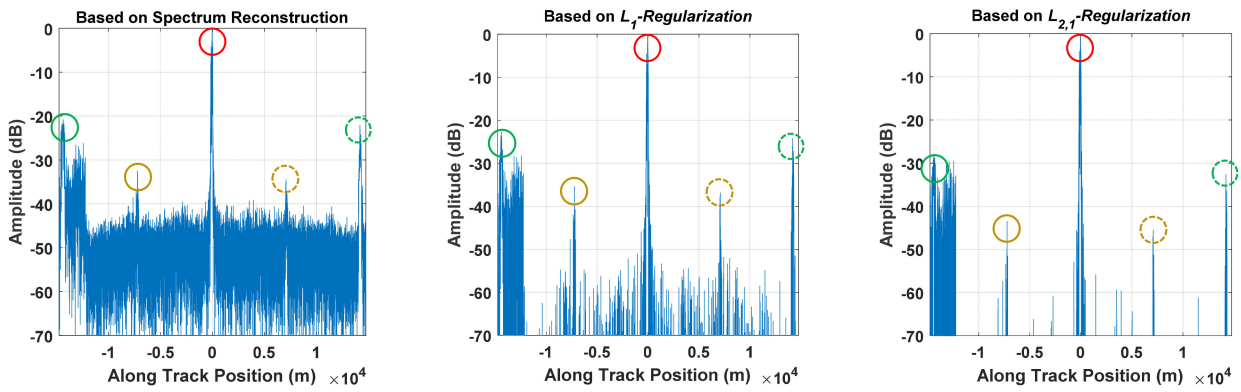

Fig. 8. Azimuth profiles of Ship 3 with three different methods. (a) SRA in [10]. (b) L_1-regularization-based method in [19]. (c) $L_{2,1}$-regularization-based method. The color and line style of the circles are corresponding to Fig. 7 and Table IV.

TABLE IV
AASR VALUE OF SHIP TARGETS BASED ON DIFFERENT METHODS [DB]

Ship	AASR$_{-1}$(brown solid line)			AASR$_{-2}$(green solid line)		
	SRA	L_1	$L_{2,1}$	SRA	L_1	$L_{2,1}$
Ship 1	-35.74	-39.53	-49.26	-22.19	-24.01	-33.73
Ship 2	-32.55	-34.91	-46.82	-27.28	-28.93	-40.66
Ship	AASR$_{+1}$(brown dash line)			AASR$_{+2}$(green dash line)		
	SRA	L_1	$L_{2,1}$	SRA	L_1	$L_{2,1}$
Ship 3	-32.24	-35.97	-44.31	-21.15	-23.74	-32.68
Ship 4	-34.11	-36.86	-49.42	-26.21	-27.54	-40.85

and AASR_{-2} are –37.38 and –24.35 dB, respectively. In the reconstructed image of the proposed $L_{2,1}$- regularization-based method Fig. 6(c), we can see that both $\pm 1\mathrm{st}$ and $\pm 2\mathrm{nd}$ ambiguities of the target are suppressed significantly, with AASR_{-1} and AASR_{-2} being –46.27 and –33.19 dB, respectively. Therefore, we can conclude that the $L_{2,1}$- regularization-based method can better suppress the azimuth ambiguities caused by nonuniform undersampling and improve the imaging quality of the Gaofen-3 dual-channel product.

In order to illustrate the azimuth ambiguities suppression ability of the proposed method in scenarios with multiple targets, in the second experiment, we compare the imaging results of SRA [10], the L_1-regularization-based method [19], and the $L_{2,1}$- regularization-based method, as shown in Fig. 7. The azimuth and range directions are marked in Fig. 7(a). We select four ships as the performance test regions, named Ship 1–Ship 4, as shown in the corresponding red circles. The $\pm 1\mathrm{st}$ ambiguous areas are marked by the brown circles with dash lines and solid lines, respectively, and the $\pm 2\mathrm{nd}$ ambiguous areas are marked by the green circles with dash lines and solid lines, respectively. The $+1\mathrm{st}$ and $+2\mathrm{nd}$ ambiguous areas of Ship 1 and Ship 2 are not marked due to their weak ambiguous energy.

Table IV describes the AASR values of Ship 1–Ship 4 in different ambiguous areas based on SRA, L_1 regularization and $L_{2,1}$ regularization, respectively. It can be seen that compared with the L_1-regularization-based method, $L_{2,1}$- regularization-based method can reduce the AASR values of different ambiguous areas by more than 10 dB, which is consistent with the simulation results. Fig. 8 shows the azimuth profiles of Ship 3 of three different methods. From Fig. 8(b) and (c), it can be seen that both the L_1-regularization-based method and $L_{2,1}$-regularization-based method can increase the TBR value by more than 15 dB. However, the L_1-regularization-based method cannot deal with the azimuth ambiguities caused by nonuniform undersampling effectively, failing to recover the target scene accurately. The $L_{2,1}$-regularization-based method takes the ambiguous areas into account when establishing the sparse SAR imaging model and utilizes the group sparsity constraint when recovering the target scene, which can suppress the azimuth ambiguities significantly. Therefore, for the nonuniform undersampling case of the azimuth multichannel SAR system, the considered scene can be reconstructed more accurately by the proposed $L_{2,1}$-regularization-based method [see Fig. 7(c)].

V. CONCLUSION

Limited by the beam position design of the spaceborne multichannel SAR systems, sometimes the PRF of each channel is less than that of uniform sampling, which will result in nonuniform undersampling. By introducing sparse signal processing theory into multichannel SAR imaging, the L_q-regularization-based method can suppress noise and sidelobes, improving the image quality. However, this method cannot resolve the azimuth ambiguities caused by nonuniform undersampling. In this article, a novel multichannel SAR imaging method for nonuniform undersampling based on $L_{2,q}$ regularization is proposed. The proposed method combines the group sparsity property with multichannel SAR data processing operators to achieve effective ambiguity suppression and computational efficiency. We analyze the factors of azimuth ambiguities in nonuniform

undersampling multichannel systems and construct the sparse SAR imaging model containing four ambiguous areas, which is different from that in single-channel systems. Then, inspired by the idea of approximated observation, the multichannel SAR data processing operators of the main imaging area and ambiguous areas are constructed to replace the observation matrices in the imaging model. Finally, by utilizing the sparse group thresholding iteration function, the target scene can be effectively recovered by solving $L_{2,q}$ regularization problem. Compared with the azimuth ambiguities suppression method in the single-channel SAR systems, the proposed method establishes the multichannel sparse SAR imaging model and SAR data processing operators that are different from those in single-channel SAR systems. We also introduce the group sparsity property into multichannel SAR data processing. The proposed method can efficiently suppress the azimuth ambiguities caused by the nonuniform undersampling. The simulation and Gaofen-3 SAR data experiment results demonstrate its validity.

APPENDIX A

Let $H_j(f)$ denote the transfer function of the jth channel, then the transfer matrix of the multichannel SAR system with M channels can be represented as follows:

$$\boldsymbol{H}(f) = \begin{bmatrix} H_1(f) & \cdots & H_M(f) \\ H_1(f+PRF) & \cdots & H_M(f+PRF) \\ \vdots & \ddots & \vdots \\ H_1(f+(M-1)PRF) & \cdots & H_M(f+(M-1)PRF) \end{bmatrix} \tag{24}$$

When the Nyquist criterion is fulfilled, the reconstruction filter matrix $\mathbf{P}(f)$ can be obtained from the inversion of the system characteristic matrix $\boldsymbol{H}(f)$, which can be expressed as follows:

$$\boldsymbol{P}(f) = \boldsymbol{H}^{-1}(f) = \begin{bmatrix} P_{11}(f) & \cdots & P_{1M}(f+(M-1)\mathrm{PRF}) \\ P_{21}(f) & \cdots & P_{2M}(f+(M-1)\mathrm{PRF}) \\ \vdots & \ddots & \vdots \\ P_{M1}(f) & \cdots & P_{MM}(f+(M-1)\mathrm{PRF}) \end{bmatrix}. \tag{25}$$

Then, we can reconstruct the Doppler spectrum of the original signal by M reconstruction filters $P_j(f)$ ($j = 1, 2, \ldots, M$), and each reconstruction filter $P_j(f)$ consists of M bandpass filters $P_{ji}(f)$ ($i = 1, 2, \ldots, M$).

APPENDIX B

Let $\mathbf{P}_i^j(f_{a,i}, \Delta x_j)$ denote the reconstruction filter matrices of the jth channel of the main imaging area ($i = 0$) and ambiguous areas ($i \neq 0$), respectively. By substituting different $f_{a,i}$ into (24) and (25), we can obtain $\mathbf{P}_i^j(f_{a,i}, \Delta x_j)$ in different areas. Let $\mathbf{\Theta}_i^{sc}(f_{a,i}, \tau) \in \mathbb{C}^{N_a \times N_r}$, $\mathbf{\Theta}_i^{rc}(f_{a,i}, f_\tau) \in \mathbb{C}^{N_a \times N_r}$, and $\mathbf{\Theta}_i^{ac}(f_{a,i}, \tau) \in \mathbb{C}^{N_a \times N_r}$ denote the chirp scaling operation, bulk RCMC, range compression and secondary range compression (SRC) operation, and azimuth focusing and phase compensation operation in CSA [26], respectively. They can be represented as follows:

$$\mathbf{\Theta}_i^{sc}(f_{a,i}, \tau) = \exp\left\{-j\pi K_s(f_{a,i}, r_{\mathrm{ref}}) C_s(f_{a,i}) \cdot \left[\tau - \frac{2}{c} r_{\mathrm{ref}}(1 + C_s(f_{a,i}))\right]^2\right\} \tag{26}$$

$$\mathbf{\Theta}_i^{rc}(f_{a,i}, f_\tau) = \exp\left\{-j\pi \frac{{f_\tau}^2}{K_s(f_{a,i}, r_{\mathrm{ref}})(1 + C_s(f_{a,i}))}\right\} \cdot \exp\left\{j\frac{4\pi}{c} f_\tau r_{\mathrm{ref}} C_s(f_{a,i})\right\} \tag{27}$$

$$\mathbf{\Theta}_i^{ac}(f_{a,i}, \tau) = \exp\left\{-j\frac{2\pi}{\lambda} c\tau(1 - D(f_{a,i}, V_r))\right\} \cdot \exp\left\{j\frac{4\pi}{c^2} K_s(f_{a,i}, r_{\mathrm{ref}})(1 + C_s(f_{a,i})) C_s(f_{a,i})(r - r_{\mathrm{ref}})^2\right\} \tag{28}$$

where $i = 0$ denotes the main imaging area; $i \neq 0$ denotes the ambiguous areas; f_τ is the range frequency; r_{ref} is the reference slant range; r is the slant range; $K_s(f_{a,i}, r)$ is the modified chirp rate in range of different areas, denoted as follows:

$$K_s(f_{a,i}, r) = \frac{K_r}{1 + K_r \frac{2r\lambda(1 - D(f_{a,i}, V_r)^2)}{c^2 \cdot D(f_{a,i}, V_r)^3}} \tag{29}$$

with

$$D(f_{a,i}, V_r) = \sqrt{1 - \left(\frac{\lambda f_{a,i}}{2V_r}\right)^2} \tag{30}$$

where V_r is the platform velocity; and $C_s(f_{a,i})$ is the curvature factor of different areas

$$C_s(f_{a,i}) = \frac{1}{D(f_{a,i}, V_r)} - 1. \tag{31}$$

ACKNOWLEDGMENT

The authors would like to thank the China Center For Resources Satellite Data and Application for providing the Gaofen-3 data.

REFERENCES

[1] R. Pelich, N. Longépé, G. Mercier, G. Hajduch, and R. Garello, "AIS-based evaluation of target detectors and SAR sensors characteristics for maritime surveillance," *IEEE J. Sel. Topics Appl. Earth Observ. Remote Sens.*, vol. 8, no. 8, pp. 3892–3901, Aug. 2014.

[2] G. Wiseman, H. McNairn, S. Homayouni, and J. Shang, "RADARSAT-2 polarimetric SAR response to crop biomass for agricultural production monitoring," *IEEE J. Sel. Topics Appl. Earth Observ. Remote Sens.*, vol. 7, no. 11, pp. 4461–4471, Nov. 2014.

[3] E. Makhoul, S. V. Baumgartner, M. Jäger, and A. Broquetas, "Multichannel SAR-GMTI in maritime scenarios with F-SAR and TerraSAR-X sensors," *IEEE J. Sel. Topics Appl. Earth Observ. Remote Sens.*, vol. 8, no. 11, pp. 5052–5067, Nov. 2015.

[4] S. Song, B. Xu, and J. Yang "Ship detection in polarimetric SAR images via variational Bayesian inference," *IEEE J. Sel. Topics Appl. Earth Observ. Remote Sens.*, vol. 10, no. 6, pp. 2819–2829, Jun. 2017.

[5] A. Currie and M. A. Brown, "Wide-swath SAR," in *Proc. Inst. Elect. Eng.—Radar, Sonar, Navigation*, vol. 139, no. 2, pp. 122–135, 1992.

[6] I. Sikaneta, C. H. Gierull, and D. Cerutti-Maori, "Optimum signal processing for multichannel SAR: With application to high-resolution wide-swath imaging," *IEEE Trans. Geosci. Remote Sens.*, vol. 52, no. 10, pp. 6095–6109, Oct. 2014.

[7] S. V. Baumgartner and G. Krieger "Simultaneous high-resolution wide-swath SAR imaging and ground moving target indication: Processing approaches and system concepts," *IEEE J. Sel. Topics Appl. Earth Observ. Remote Sens.*, vol. 8, no. 11, pp. 5015–5029, Nov. 2015.

[8] B. Han *et al.*, "The GF-3 SAR data processor," *Sensors*, vol. 18, no. 3, 2018, Art. no. 835.

[9] J. Sun, W. Yu, and Y. Deng, "The SAR payload design and performance for the GF-3 mission," *Sensors*, vol. 17, no. 10, 2017, Art. no. 2419.

[10] G. Krieger, N. Gebert, and A. Moreira, "Unambiguous SAR signal reconstruction from nonuniform displaced phase center sampling," *IEEE Geosci. Remote Sens. Lett.*, vol. 1, no. 4, pp. 260–264, Oct. 2004.

[11] J. L. Brown, "Multi-channel sampling of low-pass signals," *IEEE Trans. Circuits Syst.*, vol. 28, no. 2, pp. 101–106, Feb. 1981.

[12] N. Gebert, "Multi-channel azimuth processing for high-resolution wide-swath SAR imaging," Ph.D. dissertation, Dept. Electron. Eng. Inf. Technol., KIT, Karlsruhe, Germany, 2009.

[13] D. L. Donoho, "Compressed sensing," *IEEE Trans. Inf. Theory*, vol. 52, no. 4, pp. 1289–1306, Apr. 2006.

[14] E. J. Candes and T. Tao "Near-optimal signal recovery from random projections: Universal encoding strategies," *IEEE Trans. Inf. theory*, vol. 52, no. 12, pp. 5406–5425, Dec. 2006.

[15] B. Zhang, W. Hong, and Y. Wu, "Sparse microwave imaging: Principles and applications," *Sci. China Inf. Sci.*, vol. 55, no. 8, pp. 1722–1754, 2012.

[16] M. Çetin *et al.*, "Sparsity-driven synthetic aperture radar imaging: Reconstruction, autofocusing, moving targets, and compressed sensing," *IEEE Signal Process. Mag.*, vol. 31, no. 4, pp. 27–40, Jul. 2014.

[17] J. Fang, Z. Xu, B. Zhang, W. Hong, and Y. Wu, "Fast compressed sensing SAR imaging based on approximated observation," *IEEE J. Sel. Topics Appl. Earth Observ. Remote Sens.*, vol. 7, no. 1, pp. 352–363, Jan. 2013.

[18] H. Bi, B. Zhang, X. X. Zhu, C. Jiang, and W. Hong, "Extended chirp scaling-baseband azimuth scaling-based azimuth–range decouple L_{1} regularization for TOPS SAR imaging via CAMP," *IEEE Trans. Geosci. Remote Sens.*, vol. 55, no. 7, pp. 3748–3763, Jul. 2017.

[19] X. Quan *et al.*, "Unambiguous SAR imaging for nonuniform DPC sampling: LQ regularization method using filter bank," *IEEE Geosci. Remote Sens. Lett.*, vol. 13, no. 11, pp. 1596–1600, Nov. 2016.

[20] D. Baron, M. F. Duarte, M. B. Wakin, S. Sarvotham, and R. G. Baraniuk *et al.*, "Distributed compressive sensing," 2009, *arXiv preprint arXiv:0901.3403*, 2019. [Online]. Available: http://arxiv.org/abs/0901.3403

[21] B. Zhang, C. Jiang, and Z. Zhang, "Azimuth ambiguity suppression for SAR imaging based on group sparse reconstruction," in *Proc. 2nd Int. Workshop Compressed Sens. Appl. Radar*, Bonn, Germany, 2013, pp. 17–19.

[22] E. J. Candes and T. Tao, "Decoding by linear programming," *IEEE Trans. Inf. Theory*, vol. 51, no. 12, pp. 4203–4215, Dec. 2005.

[23] I. Daubechies, M. Defrise, and C. De Mol, "An iterative thresholding algorithm for linear inverse problems with a sparsity constraint," *Commun. Pure Appl. Math.: J. Issued Courant Inst. Math. Sci.*, vol. 57, no. 11, pp. 1413–1457, 2004.

[24] G. Xu, X. G. Xia, and W. Hong, "Nonambiguous SAR image formation of maritime targets using weighted sparse approach," *IEEE Trans. Geosci. Remote Sens.*, vol. 56, no. 3, pp. 1454–1465, Mar. 2018.

[25] J. Friedman, T. Hastie, and R. Tibshirani, "A note on the group lasso and a sparse group lasso," *arXiv preprint arXiv:1001.0736*, 2010. [Online]. Available: http://arxiv.org/abs/1001.0736

[26] R. K. Raney, H. Runge, R. Bamler, I. G. Cumming, and F. H. Wong, "Precision SAR processing using chirp scaling," *IEEE Trans. Geosci. Remote Sens.*, vol. 32, no. 4, pp. 786–799, Jul. 1994.

[27] N. Rao *et al.*, "Sparse overlapping sets lasso for multitask learning and its application to FMRI analysis," *Adv. Neural Inf. Process. Syst.*, 2013, pp. 2202–2210, 2013.

[28] Z. Xu, X. Chang, F. Xu, and H. Zhang, "L_{1/2} regularization: A thresholding representation theory and a fast solver," *IEEE Trans. Neural Netw. Learn. Syst.*, vol. 23, no. 7, pp. 1013–1027, Jul. 2012.

[29] M. Çetin, W. C. Karl, and D. A. Castanon, "Feature enhancement and ATR performance using nonquadratic optimization-based SAR imaging," *IEEE Trans. Aerosp. Electron. Syst.*, vol. 39, no. 4, pp. 1375–1395, Oct. 2003.

Mingqian Liu received the bachelor's degree in electronic information engineering from the Beijing Institute of Technology, Beijing, China, in 2017. He is currently working toward the Ph.D. degree in signal and information processing with the University of Chinese Academy of Sciences, Beijing, China.

His main research interests include radar signal processing, compressed sensing and sparse SAR imaging.

Bingchen Zhang was born in 1973. He received the bachelor's degree in electronic engineering and information science from the University of Science and Technology of China, Hefei, China, in 1996, and the master's and Ph.D. degrees from the Institute of Electronics, Chinese Academy of Sciences (IECAS), Beijing, China, in 1999 and 2017, respectively.

Since 1999, he has been a Scientist with IECAS. His main research interests include synthetic aperture radar (SAR) signal processing and airborne SAR system design, implementation, and data processing.

Zhongqiu Xu received the bachelor's degree in detection guidance and control techniques from the Beijing Institute of Technology, Beijing, China, in 2018. He is currently working toward the Ph.D. degree in signal and information processing with the University of Chinese Academy of Sciences, Beijing, China.

His main research interests include radar signal processing, compressed sensing, and sparse SAR imaging.

Yan Zhang received the bachelor's degree in electronic information engineering from the Dalian University of Technology, Dalian, China, in 2018. He is currently working toward the Ph.D. degree in signal and information processing with the University of Chinese Academy of Sciences, Beijing, China.

His main research interests include automotive radar signal processing and compressed sensing.

Lihua Zhong received the bachelor's degree in electronic engineering from Beihang University, Beijing, China, in 2007, and the Ph.D. degree in signal and information processing from the University of Chinese Academy of Sciences, Beijing, China, in 2013.

Since 2013, he has been with the Institute of Electronics, Chinese Academy of Sciences, Beijing, China. He is currently an Associate Research Fellow with Aerospace Information Research Institute, Chinese Academy of Sciences, Beijing. His research interests include synthetic aperture radar (SAR) imaging and radiometric correction.

Yirong Wu (Member, IEEE) received the MS.D. degree in microwave electromagnetic field from the Beijing Institute of Technology, Beijing, China, in 1988 and the Ph.D. degree in signal and information processing from the Institute of Electronics, Chinese Academy of Sciences (IECAS), Beijing, China, in 2001.

Since 1988, he has been with IECAS, where he currently serves as the Director. He has over 20 years of experience in remote sensing processing system design. His current research interests are microwave imaging, signal and information processing, and related applications.